Bulletin of the Seismological Society of America, Vol. 102, No. 3, pp. 1155–1166, June 2012, doi: 10.1785/0120100010

Microseismic Noise from Large Ice-Covered Lakes?

by Yu J. Gu and Luyi Shen

Abstract This study examines the background seismic noise in the southern Western Canadian Sedimentary Basin (WCSB) using broadband seismic records from Canadian Rockies and Alberta Network (CRANE) and Canadian National Seismograph Network (CNSN). The cross-correlations of vertical-component data reveal highly asymmetric Rayleigh wave signals in the frequency range of 0.02–0.2 Hz. Travel-time and waveform source migration calculations jointly suggest a persistent noise source near Lesser Slave Lake (LSL), a large ice-covered lake in Alberta, Canada, during winter months. The source origin remains unclear, though the gravity current and turbulence induced by laterally varying luminosity, ice thickness, lake depth, and lake-bottom topography could contribute to the observed microseismic signal. Seasonal variations in regional wind energy, ground attenuation, and local industrial and/or recreational activities may also affect the clarity and asymmetry of noise-correlation functions.

Introduction

For over a half century, ocean swells and shoreline–wave interactions have been known to produce detectable seismic energy in the frequency range of 0.05–0.2 Hz (Gutenberg, 1931; Longuet-Higgins, 1950; Hasselmann, 1963). These microseismic signals often exhibit strong directivity and, in some areas, seasonal or daily fluctuations (e.g., Schulte-Pelkum *et al.*, 2004; Rhie and Romanowicz, 2006; Gerstoft and Tanimoto, 2007; Webb, 2007; Kedar *et al.*, 2008; Yao and van der Hilst, 2009; Ardhuin *et al.*, 2011; Schimmel *et al.*, 2011). Distinctive amplitude asymmetries in the cross-correlation function of seismic noise (Paul *et al.*, 2005; Gu *et al.*, 2007; Yang and Ritzwoller, 2008) have revealed key characteristics of source distribution, geometry, strength, and mechanism (Stehly *et al.*, 2006; Brzak *et al.*, 2009; Koper *et al.*, 2010; Schimmel *et al.*, 2011).

Pressure fluctuations in large rivers and lakes are also capable of generating sustained seismic signals. Lynch (1956) documented the passage of storms over the Great Lakes as a potential seismic source, radiating from the lake to distances as far as North Carolina. The frequencies of the lake wave during the summer time were consistent with that of the secondary (~0.2 Hz) ocean microseism. Wind-induced lake wave microseisms (1–3 Hz) were later reported near Great Slave Lake (Weichert and Henger, 1976) and Lake Ontario (Kerman and Mereu, 1993), showing strong spectral correlations between buoy and onland seismic records. River discharge (Burtin *et al.*, 2008) and gravitational variations associated with bed load transport near geysers (Tikku *et al.*, 2006) are alternative sources and mechanisms for localized seismic signals. Similar to oceanic wave sources, motions inside lakes and rivers are highly sensitive to fluid/mass discharge, water depth, shoreline steepness/geometry, and bottom topography (Malm, 1999; Kvarnas, 2001; Wuest and Lorke, 2003; Burtin *et al.*, 2008). For large ice-covered lakes, luminosity, snow coverage, ice thickness, and resonance are also contributing factors to ground motion (e.g., Patterson and Hamblin, 1988; Kenney, 1991; Rogers *et al.*, 1995; Kenney, 1996; Kelley, 1997; Petrov *et al.*, 2007).

In this study we investigate the nature of persistent ground motion in the southwestern portion of the Western Canadian Sedimentary Basin (WCSB). Our observations reveal a local microseismic noise source near Lesser Slave Lake (LSL). The seasonal variation of the observed signals suggests potential ground motion within and around the closed water environment, that is, a frozen lake. The existence of the observed noise source and its potential connection to human or environmental factors will be carefully examined.

Noise Correlation and Remote Noise Source

This study utilizes continuous records from CRANE (Gu *et al.*, 2009), the first semipermanent broadband seismic array in Alberta, in combination with three stations from the Canadian National Seismograph Network (CNSN). Most of these receivers (Fig. 1a) operated continuously between 2007 and 2008 and provide the first semiuniform array coverage in the southern-central WCSB (see Data and Resources). The average distance between stations is approximately 180 km, which translates to a shear wave travel time of ~60 s at an average crustal speed of 3 km/s. We include additional data from 2009 to 2010 (see Fig. 1a) for improved resolution and support of key findings. For each station, we divide continuous displacement seismograms into 12-hour intervals and apply a Butterworth band-pass filter with cutoff frequencies of 0.01 Hz and 10 Hz. The resulting vertical-component seismograms for each station pair are correlated and stacked over

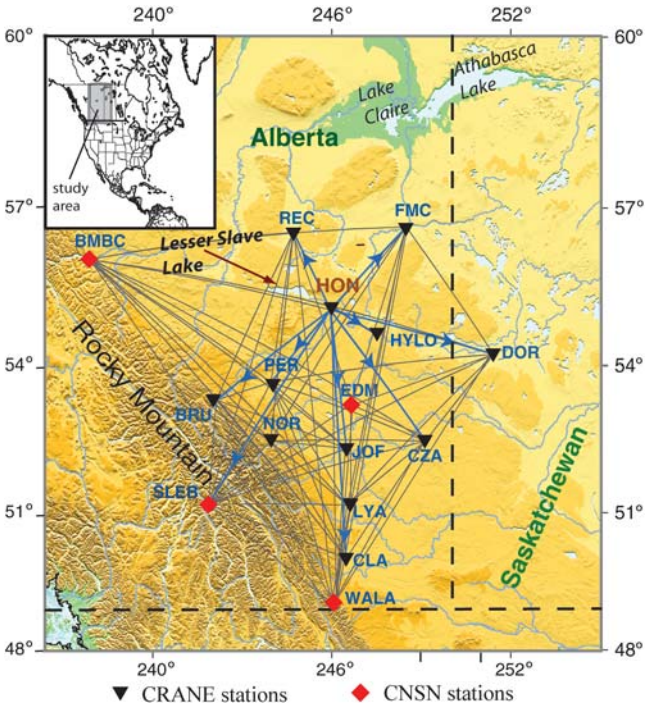

Figure 1. Distribution of stations from the Canadian Rockies and Alberta Network (CRANE, black triangles) and nearby Canadian National Seismographic Network (CNSN, red diamond). The background colors show the topography of the region. The thin gray lines connecting the stations indicate all station pairs analyzed by this study. The blue lines with arrows indicate the station pair and order (e.g., for A × B, the arrow would point to B) used in the migration analysis. The map inset shows the position of the study region relative to North America. Records from HYLO (available since June 2010) are used for waveform comparisons in Figures 3 and 9. The name of this station was changed to HLO after 6 months.

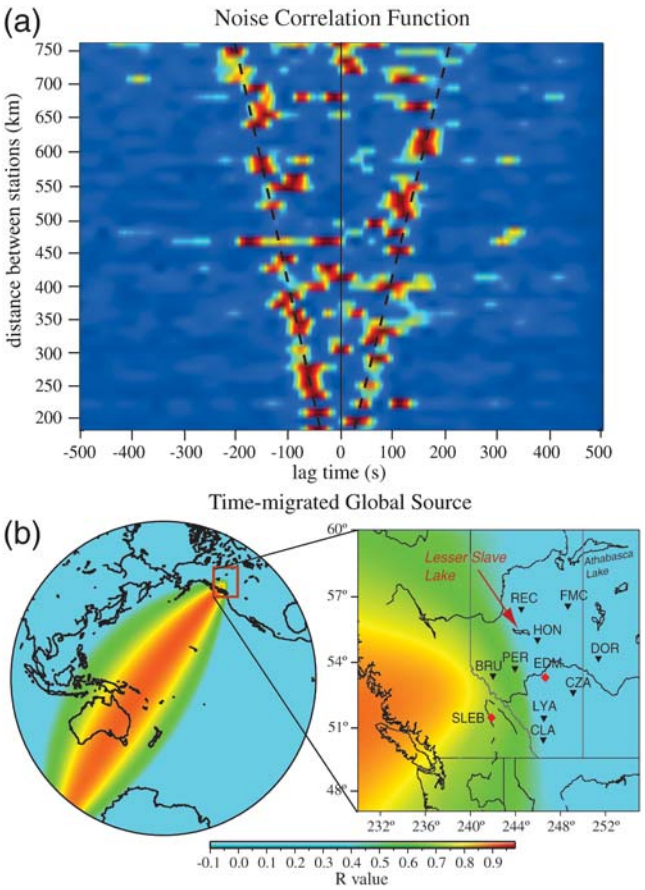

Figure 2. (a) Stacked cross-correlation functions (color-coded and slightly interpolated) for all station pairs denoted by gray lines in Figure 1. The dashed lines indicate the theoretical lag time based on a constant background velocity of 3 km/s. The lag time-distance relationship approximately follows two linear move-outs, but significant asymmetry is present on the individual correlation functions. By our sign convention, a negative lag on the SCCF of A × B implies that Rayleigh waves reaches station A first. (b) Source migration result using all station pairs connected by gray lines in Figure 1. The color scale shows the magnitude of values (maximum = 1); a high value implies a strong probability that the true source is located at the center of the grid point under discussion. (c) A magnified view of the study region enclosed by the rectangular box in Figure 2b. A dominant noise source is observed in the Pacific Ocean southwest of the station array.

spans of 5+ months (e.g., Yang *et al.*, 2007; Bensen *et al.*, 2007; Brzak *et al.*, 2009).

A lag-time versus distance diagram based on all stacked cross-correlation functions (SCCFs) shows energetic signals resulting from propagating Rayleigh waves (e.g., Schulte-Pelkum *et al.* 2004; Shapiro *et al.*, 2005, 2006; Stehly *et al.*, 2006; Gerstoft and Tanimoto, 2007; Bensen *et al.*, 2007; Koper *et al.*, 2010) (Fig. 2a). By our sign convention, a negative lag from correlating stations A (from here on, anchor station) with B (denoted as A × B) implies that noise energy consistently reaches station A prior to B. Symmetric SCCFs are generally interpreted as evidence of ambient background noises (e.g., Shapiro *et al.*, 2005; Bensen *et al.*, 2007; Yang *et al.*, 2007; Yao and van der Hilst, 2009), whereas asymmetry reflects biased source distributions relative to the receiver geometry (e.g., Paul *et al.*, 2005; Gu *et al.*, 2007; Yang and Ritzwoller, 2008; Brzak *et al.*, 2009; Schimmel *et al.*, 2011). Despite a random selection of the anchor station in each station pair, a procedure that tends to enhance the symmetric appearance of SCCFs, the majority of the station pairs are highly asymmetric upon a trace-by-trace examination.

We utilize both time and waveform migration methods to determine the locations and strengths of potential noise sources. The study region (see Fig. 1) is partitioned into equal-area ($0.5^\circ \times 0.5^\circ$) cells containing hypothetical noise sources. For each cell, the time-based migration approach defines a quantity R based on the residual lag time between predicted and observed SCCF peaks,

$$R = 1 - \frac{1}{M \times N} \sum_{i=1}^{M} \sum_{j=1}^{N} \left\{ \frac{[\Delta_i(x,y) - \Delta_j(x,y)]/v_g}{T_{ij}} - 1 \right\}^2, \quad (1)$$

where M and N are the number of stations ($M = 1$, if the migration is performed on station pairs with the same

anchor), and v_g is the average Rayleigh wave group velocity. Distances from a hypothetical source positioned at (x, y) to the i-th and j-th stations are represented by $\Delta_i(x, y)$ and $\Delta_j(x, y)$, respectively. Finally, T_{ij} (a scalar quantity) denotes the observed lag time of the noise-correlation peak in the SCCF of the i-th and j-th stations. In essence, R represents the normalized probability that a hypothetical source in cell (x, y) coincides with the true source location. This method depends solely on the lag times of noise-correlation peaks and will henceforth be referred to as time migration (e.g., Shapiro *et al.*, 2006).

To incorporate noise-correlation amplitude information and verify/refine the results of time migration, we define an independent migration time series $\mathbf{A}(t)$ where

$$\mathbf{A}(t) = \frac{1}{M \times N} \sum_{i=1}^{M} \sum_{j=1}^{N} \mathbf{X}_{ij} \left[t + \frac{\Delta_i(x, y) - \Delta_j(x, y)}{v_g} \right]. \quad (2)$$

The definitions of M, N, v_g, and Δ in this formulation remain unchanged from equation (1). For each cell position (x, y), the summation is now performed over time-shifted correlation stack $\mathbf{X}_{ij}(t)$ for a lag time of t. This formulation is similar to methods adopted by Rhie and Romanowicz (2006) and Brzak *et al.* (2009), as the time shift to each correlation stack is governed by the relative distances from a source at (x, y) to the i-th and j-th stations divided by the group velocity v_g. Finally, the maximum absolute amplitude of $\mathbf{A}(t)$ is used as an effective measure of the probability that the true noise source is located in a given cell.

The initial choice of v_g is based on the average shear velocity model of Gu *et al.* (2009) using teleseismic body wave data from the same array. The time migration of all station pairs for the entire frequency window shows large R values west-southwest of the station formation (Fig. 2b), highlighting the positive half of a great-circle path in the Pacific Ocean (Fig. 2b). The global maximum is observed near Tonga–Fiji region, which is in the vicinity of a dominant global noise source in Yang and Ritzwoller (2008). This potential source location is away from the nearest shoreline, thus favoring a mechanism involving nonlinear interactions of ocean waves (Longuet-Higgins, 1950; Hasselmann, 1963; Haubrich and McCamy, 1969; Hughes, 1976; Chevrot *et al.*, 2007). However, caution has to be exercised regarding this interpretation because only the source orientation could be determined with acceptable accuracy by the small-aperture receiver array. The insufficient data constraint on distance implies that potential noise sources originating from Hawaii (Schimell *et al.*, 2011) and Pacific coastal ranges (e.g., near Vancouver Island) cannot be excluded.

Local Microseismic Noise Source

Travel-Time Migration

The primary focus of this study is a second, local source within the WCSB. The lag times of correlation peaks at a number of stations are incompatible with those expected from noise sources in the Pacific Ocean. For example, the SCCF of stations HON × DOR (Fig. 3a) is symmetric at low frequencies (0.01–0.06 Hz) and high frequencies (> 0.19 Hz), but the intermediate frequencies are dominated by strong correlation peaks with large negative lag times. Based on the orientation of the migrated global source

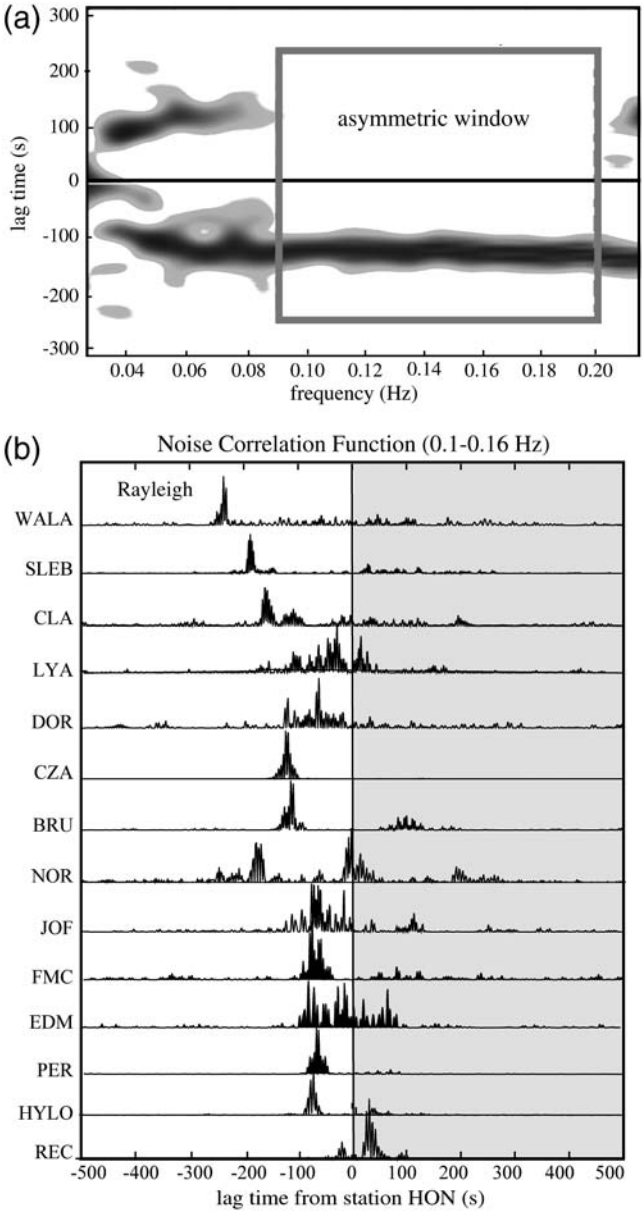

Figure 3. (a) Vertical-component cross-correlation of station HON (anchor) and DOR for a cutoff frequency range of 0.01–0.2 Hz. The SCCF is computed by a series of narrow band-pass filters within the frequency range of interest. The move-out curve is symmetrical at both low and high frequencies but shows strong asymmetry in the range of 0.08–0.16 Hz. (b) Normalized absolute values of SCCFs of station pairs anchored by HON. The shaded region highlights the positive lag times, which roughly follow a semi-linear relationship. With the exception of HYLO, all SCCFs are used in regional source migrations.

(Pacific Ocean southwest of station array, see Fig. 2b), the absolute lag time of this asymmetric peak (> 100 s) well exceeds the time difference associated with paths connecting the global source with this station pair (< 50 s). In other words, an additional noise source closer to HON than DOR is required to explain the observed SCCF.

The need for a secondary noise source (see Fig. 3a) is not coincidental. Similar signal characteristics are consistently observed on the SCCFs of station pairs anchored by HON (Fig. 3b). The peaks of the SCCFs anchored by HON generally become more negative in lag time with increasing station separations, which imply that the energy from persistent ground movements reaches HON prior to other stations. To determine the regional source location and minimize the effect of the global source, we perform time migration based on all quality station pairs anchored by HON (see Fig. 3b); the SCCF associated with HYLO is omitted due to insufficient data. The maximum R value from time migration (Fig. 4a) provides more quantitative support for a potential local noise source. The peak of the migration amplitude near HON nearly doubles the average values of the region north of the station array and quadruples those in southern Alberta. The uniqueness of this potential source location is evident from a comparison of three hypothetical source locations (Fig. 4b). In this hypothesis test, R values are computed for station pairs (i.e., $M = N = 1$ in equation 1), assuming a 3 km/s background velocity and a hypothetical source at the anchor station (HON, CZA, and CLA are used as anchors for this test). The R value at a given station is inversely proportional to the time difference between the predicted and observed lag times, and the average associated with a hypothetical source at HON is 0.6–0.8 higher than that of the two remaining source locations (see Fig. 4b). In fact, the only large R values from hypothetical sources away from HON (e.g., CZA in blue, Fig. 4b) are results of autocorrelation (defaulted to 1) (see Fig. 4b).

The main source of uncertainty is the assumed Rayleigh wave group velocity during travel-time migration. The subjective choice of a constant average velocity for the study region can introduce errors to the source location due to (1) crust and mantle 3D heterogeneities and (2) difficulties in accommodating dispersive surface waves with a single 1D velocity. Heterogeneous path effects are clearly demonstrated by an anomalously delayed peak in the SCCF of HON × NOR (see Fig. 3b), where shear wave velocity is ~10–15% slower than the regional average based on a preliminary analysis of the same data set (Gu *et al.*, 2011). Unfortunately, reliable crust and mantle velocity models of WCSB remain a work-in-progress, largely owing to the lack of receivers prior to the establishment of CRANE. We repeat the experiment shown in Figure 3a with a wide range of migration velocities to assess the source location dependency on velocity. Figure 4c shows the distances between the resulting source locations and a reference point in the eastern bay of LSL, a potential source location. Mislocations range from 30 to 100 km for all selected migration velocities. Within a realistic group velocity range of 2.5–3.4 km/s (Gu *et al.*, 2011), mislocations decrease with increasing velocities but stabilize at large v_g values. The latter observation can be

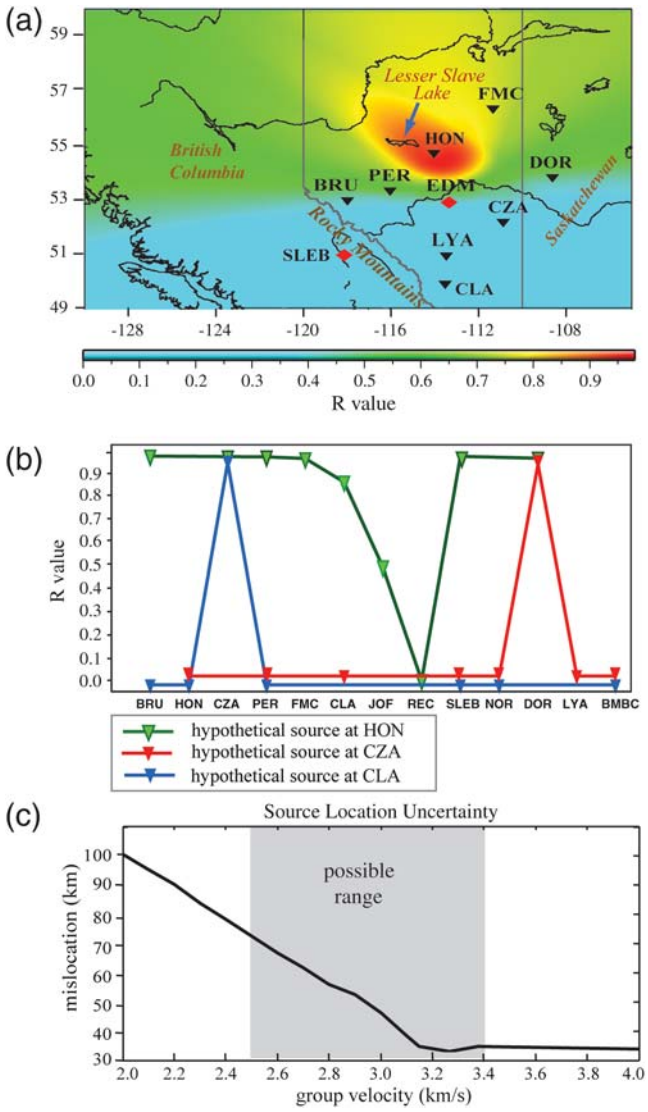

Figure 4. (a) Time-migrated R values of the study region. A cell with a large R value implies a strong possibility of containing the true noise source. The maximum R value is observed near LSL, though the precision of the noise source location is limited by station density. (b) Values of station pairs based on a background Rayleigh wave group velocity of 3.0 km/s and hypothetical noise sources at the station locations of HON (green), CZA (red) and CLA (blue), respectively. As a simple example, R for a hypothetical source at CZA (also the location of the anchor station) and station NOR (plotted as a red inverted triangle) is computed based on equation (1) while assuming (1) $M = N = 1$, and (2) T_{ij} is the observed lag-time of the SCCF between CZA (anchor station and hypothetical source) and NOR. The inverted triangles indicate station pairs with robust noise-correlation peaks and stations that resulted in poor correlations with the majority of the three anchors (e.g., WALA) are omitted. (c) Migration results based on background velocities ranging from 2.0 to 4.0 km/s. The vertical axis shows the distance between the resulting noise source location and reference point in the east basin of LSL. The shaded region marks the range of realistic background velocities ranging from 2.5 to 3.4 km/s (Gu *et al.*, 2011).

attributed to decreased imaging resolution when the Rayleigh wave travel-time differences between station pairs become negligible under unrealistically large wave speeds. Considering the limited number of stations, coarse migration grid size and errors associated with 1D approximation, a realistic estimate of location uncertainty is 60–100 km from the reference position.

Location uncertainty is negatively impacted by the SCCFs associated with stations BMBC and REC. First, the results of BMBC are inconsistent with signatures from all three hypothetical sources (Fig. 4b), which may be caused by (1) low signal qualities at large distances from the optimal location of the regional source, and/or (2) competing source effects from the Pacific Ocean. Low data quality also affects REC, as the SCCFs from four adjacent station pairs anchored by REC (NOR, PER, EDM, BRU) show little, if any, indications of correlated background noise (Fig. 5). Station REC was extracted prematurely within a year of operation due to severe water damages to the instrument vault. While the source of flooding was later determined to be a catastrophic failure involving local frost heaves, the impact of vault condition deterioration on the data recorded prior to the failure remains uncertain. Still, the robust signal from the SCCF of REC × HON is unlikely to be instrument related (see Fig. 5). The sign of the lag time indicates that noise energy reaches REC first, which would require a short path to REC and/or a slow path to HON. Both conditions can be satisfied if the true noise source resides within the west bay of LSL: in addition to a slightly greater distance to HON than to REC, energy from this potential source needs to travel the full length of LSL across a seismically slow layer containing water, ice (if in winter), and thick lake sediments. Validation of this hypothesis would, however, require further improvements to the existing source location.

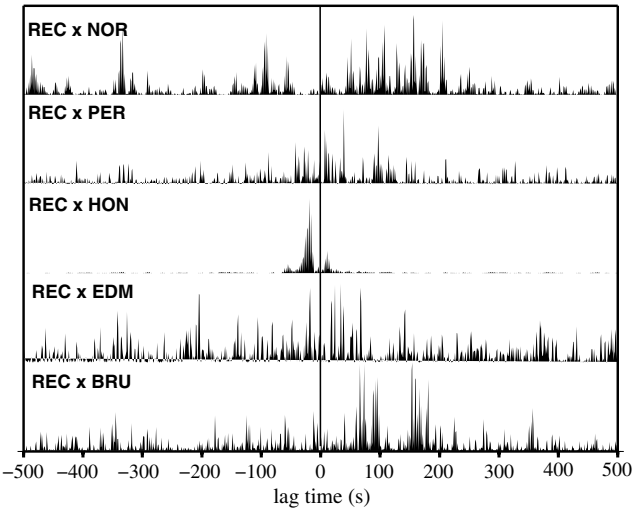

Figure 5. Sample noise-correlation stacks computed from REC (anchor) and five nearby stations. Low signal-to-noise ratios are observed on four stations, which reflects data quality issues. The final correlation pair (REC × HON) provides additional information on the location of the potential regional noise source (see main text).

Waveform Migration

The addition of waveform information based on equation (2) provides further evidence of a persistent microseismic source near LSL. Based on station pairs anchored by HON and an average group velocity of 3.0 km/s (Gu *et al.*, 2011), the result of waveform migration shows an elongated high-probability zone in the western part of the station array (Fig. 6). A local amplitude maximum is observed in north-central LSL, which is approximately 80–100 km northwest of the regional maximum from the time migration (see Fig. 4a) and the amplitude nearly doubles those in southeastern Alberta. The location and strength of the noise source are moderately dependent on the 1D migration velocity (Fig. 7). For instance, the choices of $v_g = 2.5$ km/s and $v_g = 2.9$ km/s result in strong migration amplitudes around LSL, whereas $v_g = 3.1$ km/s tends to shift the local maximum to the southwest by 100–120 km. A rough estimate of the location uncertainty is 80–120 km, with the respective

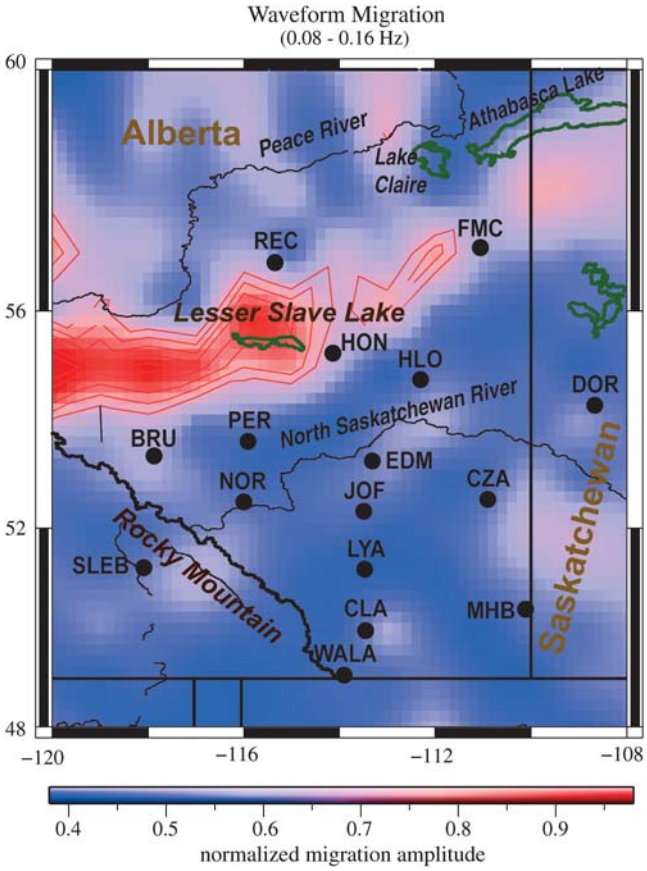

Figure 6. Result of waveform migration based on equation (2). The SCCFs were filtered between 0.08 Hz and 0.16 Hz prior to migration, and the background Rayleigh wave group velocity was set at 3.0 km/s. Large migration amplitudes are observed near LSL, potentially extending to the western boundary of our study region.

uncertainties of ~100 km and ~50 km in longitude and latitude (see Fig. 7).

Large migration amplitudes near the western boundary of the study region, especially for cases where $v_g <$ 2.9 km/s, underscore a key difference between the outcomes of time and waveform migrations. For time migration, the influence of global sources is minimized by restricting the analysis to the subset of station pairs anchored by HON (see Fig. 4a). This approach is not nearly as effective in waveform migration due to the complexity and sensitivity of correlation amplitudes. The anomalously high migration amplitudes near the western boundary of the study region show no visible signs of decay. In view of the low sensitivity of SCCFs to distance, this observation could be caused by a remote noise source outside of the study region. The projected orientation of this source (west) differs with that suggested by time migration approach (southwest, see Fig. 2b), thus raising questions about the existence of a second global source away from the study region. In the case of waveform migration, the Pacific coast of Canada is an appealing landward entry point of the source energy resulting from either coastal impact or pelagic sources (e.g., Schulte-Pelkum *et al.*, 2004; Shapiro *et al.*, 2005; Sabra *et al.*, 2005; Gerstoft and Tanimoto, 2007; Gu *et al.*, 2007; Chevrot *et al.*, 2007; Yang and Ritzwoller, 2008; Brzak *et al.*, 2009; Ardhuin *et al.*, 2011; Shimmel *et al.*, 2011). The strengths of potential global noise sources from both migration approaches are susceptible to influences from the shape and topography of associated coastlines, from atmospheric pressure and ocean swells, as well as from the ground attenuation of the land portion of great-circle paths connecting noise sources and receivers.

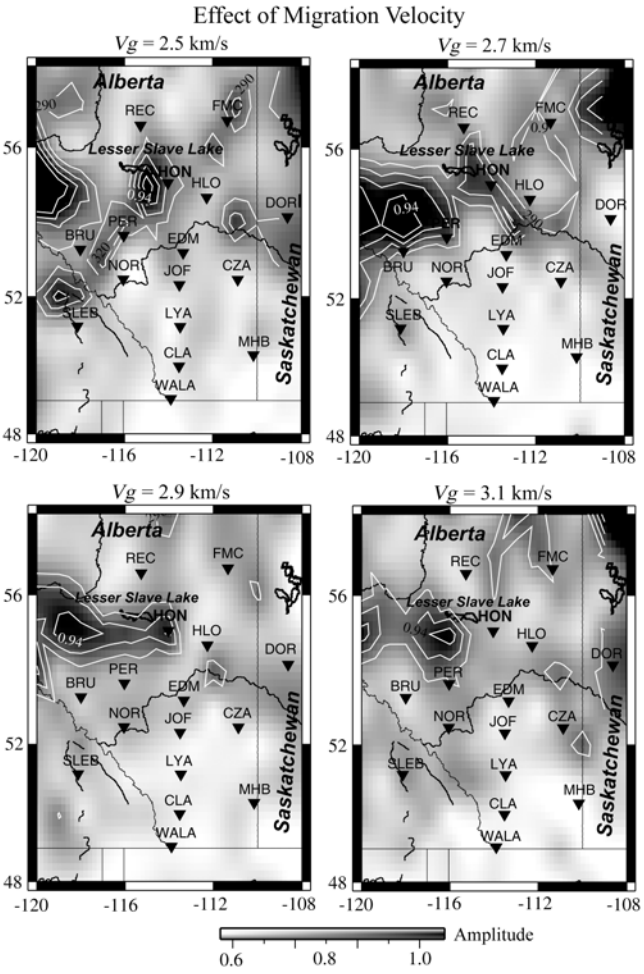

Figure 7. Waveform migration results from four different Rayleigh wave group velocities. A local maximum is consistently observed in the vicinity of LSL. The estimated location uncertainty based on the movement of the source is ~100–120 km. Effects of background velocity on source location are underscored by the large migration amplitudes near the northwestern boundary of the study region when v_g falls below ~2.7 km/s.

Frequency Dependence of Noise Energy

Seismic background noise has been recorded at frequencies ranging from a few millihertz, which is characteristic of continuous background free oscillations known as "hums of the Earth" (Suda *et al.*, 1998; Tanimoto *et al.*, 1998; Rhie and Romanowicz, 2006; Webb, 2007), to tens of hertz. Their origins remain inconclusive (Webb, 2007), though recent observations have suggested atmosphere/ocean/seafloor coupling as a major contributing factor at all frequencies (Stehly *et al.*, 2006; Rhie and Romanowicz, 2006; Shapiro *et al.*, 2006; Yang and Ritzwoller, 2008; Kedar *et al.*, 2008). The frequency band of interest in this study is (0.01–0.2 Hz), a range highlighted by energetic spectral signals at 0.05–0.08 Hz (primary microseisms) and 0.1–0.3 Hz (secondary microseisms) (Gutenberg, 1931; Longuet-Higgins, 1950; Hasselmann, 1963; Haubrick and McCamy, 1969; Hughes, 1976). The asymmetric dispersion relation exhibited by the SCCF of HON × DOR (see Fig. 3a) is, to first order, consistent with the spectral characteristics of ocean microseisms.

In order to systematically quantify the frequency dependence of asymmetric SCCFs and noise source location(s) (e.g., Frank *et al.*, 2009), we refilter the broadband datasets and repeat waveform migration over four narrow frequency bands while assuming a constant migration velocity of 3.0 km/s (Fig. 8). At a center frequency of 0.34 Hz, an isolated migration peak is detected at ~80 km distance from the western part of LSL. The strength and dimension of this high-probability zone increase substantially in the secondary microseism range (0.1–0.18 Hz), and the center of the migration peak is observed less than 50 km away from LSL (see Fig. 8). The strength of the same migration peak remains significant at primary microseism frequencies (0.06–0.14 Hz), though the global maximum amplitude shifts to the northwestern part of the study region at ~56° latitude. Despite these differences, however, the main observations from all three aforementioned frequency ranges are consistent and suggest a common local source with overlapping frequencies to those of ocean microseisms. The migration results severely degrade at the center frequency of 0.05 Hz (see Fig. 8),

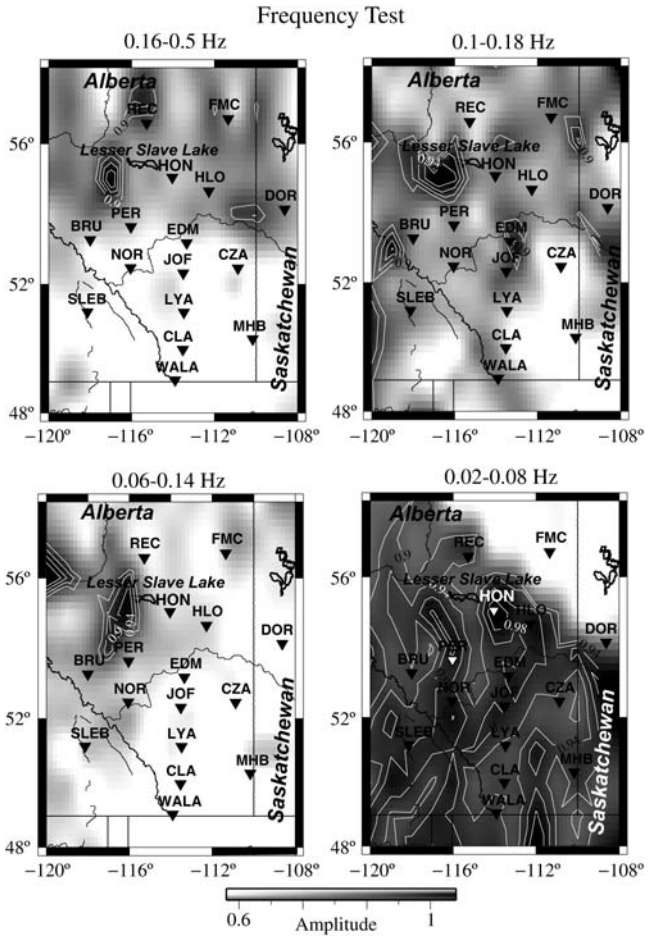

Figure 8. Waveform migration results from four slightly overlapping frequency bands. Strong migration amplitudes are observed near the west bay of LSL, particularly in the typical frequency range of ocean microseisms (0.06–0.18 Hz). The effect of the local noise source is minimal at longer periods (0.02–0.08 Hz, bottom right) as noise-correlation functions become increasingly symmetric.

where a local maximum near the southeastern part of LSL is only marginally above the regional average. This characteristic change from other frequencies can be attributed to increasingly symmetric correlation functions, as demonstrated in Figure 3a, at frequencies below ~0.06 Hz.

Discussion

Asymmetric SCCFs have been widely observed (e.g., Schulte-Pelkum *et al.*, 2004; Shapiro *et al.*, 2005; Sabra *et al.*, 2005; Gerstoft and Tanimoto, 2007; Gu *et al.*, 2007; Yang and Ritzwoller, 2008; Ardhuin *et al.*, 2011) and numerically simulated (Stehly, 2006; Chevrot *et al.*, 2007; Kedar *et al.*, 2008; Brzak *et al.*, 2009; Ardhuin *et al.*, 2011; Shimmel *et al.*, 2011) in recent years. In most cases, amplitude symmetry can be associated with preferred directionality of the noise field surrounding stations (Frank *et al.*, 2009). This study is predicated on this premise and, despite notable differences in the outcomes, our travel-time and waveform migrations of SCCFs from a regional broadband array jointly suggest a local noise source in the vicinity of LSL. A simple demonstration of the noise source is presented in Figure 9. In this example, four station pairs anchored by HON form two azimuth bins separated by ~90° angle (Fig. 9a). The high-quality SCCFs computed from four years of continuous recordings (2007–2010) show pronounced asymmetric correlation peaks with negative signs, which imply (1) noise energy from each potential source reaches HON prior to other stations, and (2) the additional distances traveled by the noise energy after reaching HON are comparable to station

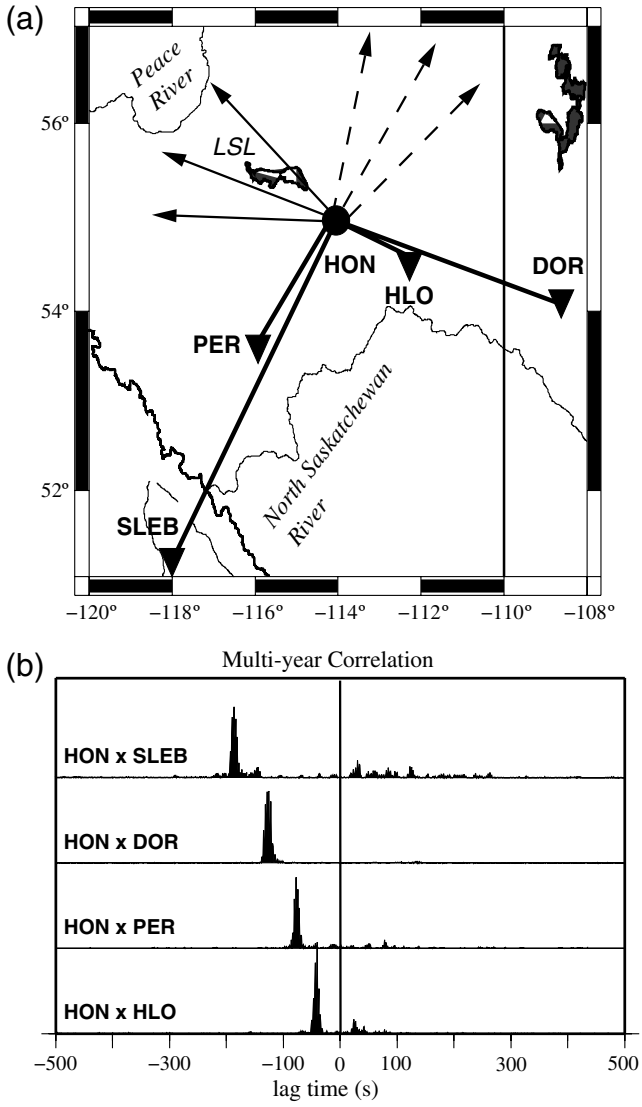

Figure 9. (a) Geographical location and path coverage provided by HON and four nearby stations. The solid and dotted lines with arrows indicate the expected source orientations based on the signs (all negative) and lag times of the SCCF maxima. (b) SCCFs computed for station pairs shown in (a) based on recordings from 2007 to 2010. The high quality SCCFs show pronounced asymmetric correlation peaks with negative signs. In view of the unique geometries of these stations, a single local noise source must be present in the vicinity, preferably in the northwest, of HON.

separations. Mechanisms involving two independent global/remote sources (e.g., Chevrot *et al.*, 2007; Yang and Ritzwoller, 2008; Pawlak *et al.*, 2011) can satisfy the timing requirements from the SCCFs, but multiple sources oriented nearly perpendicularly to each other should also produce distinctive correlation peaks on each SCCF. The latter assumption is clearly at odds with the vast majority of SCCFs shown in Figure 9. As the only viable alternative, a single source is required in the vicinity (preferably to the northwest) of HON based on the path geometries.

A broad range of environmental factors including oil/gas surveys, natural ground motion, and water flow could contribute to the observed microseisms near HON/LSL. We hereby assess the importance of each factor based on the existing knowledge about the potential source region and the characteristics of the observed SCCFs. First, the frequency of ground motion caused by active oil/gas surveys or logging activities are generally greater than 5 Hz (Yilmaz, 2001), which is significantly higher than the observed asymmetrical frequency range (0.08–0.15 Hz). More importantly, based on the published report of industrial activity by Alberta Energy in 2009, major projects have been ongoing at oil/gas hotspots such as Fort McMurray, Cold Lake, and Peace River in Alberta, Canada. Should exploration activities be responsible for source migration amplitude and SCCF asymmetry, the expected severity of ground movements in the vicinity of these hotspots would be comparable to, if not greater than, that near LSL. Unfortunately, this assumption is not supported by the observed SCCFs and source locations inferred from Figures 4 to 9.

Questions of uniqueness are equally valid for known geological processes such earthquakes or continuous creep (Brooker and Peck, 1993; Mansour, 2009) in response to stress accumulation and release in the WCSB. Earthquakes up to M_w 5.5 have previously been recorded in Alberta according to Earthquake Canada (see Data and Resources), though known activities in the vicinity of HON have been limited to date. A recent study based on CRANE and nearby permanent stations (Stern and Gu, 2011) shows that most of the recent regional microseismicities are concentrated along the Rocky Mountain foothills and southernmost Alberta. Other detectable events such as mining blasts (e.g., Wabamum Lake; Stern and Gu, 2011) and landslides (e.g., Turtle Mountain; Brooker and Peck, 1993; Friedmann *et al.*, 2003; Pedrazzini *et al.*, 2008) and Peace River (Cruden *et al.*, 1990; Davis *et al.*, 2005; Morgan *et al.*, 2008) are simply too far from the potential noise source region to be considered major contributing factors. Still, in the absence of strong moment releases in the potential source region, the seismic potential and characteristic frequencies of continuous stress releases interweaving with the effect of ocean microseisms (Frank *et al.*, 2009) remain plausible in the vicinity of LSL.

The SCCF peak frequencies generally favor water as a key ingredient in the generation of dominant seismic noise. While the WCSB is devoid of oceans and seas, LSL and channels of the Athabasca River are both potential sources of microseisms. A comparison of independent SCCFs from the winter months (December 2007–March 2008) and summer months (May 2008–October 2008) (Fig. 10a) offers additional insights into the timing and mechanics of the noise source. The winter SCCFs are highly asymmetrical and well correlated with the observed asymmetry on the annual SCCFs. The summer SCCFs are, in comparison, significantly more symmetric (see Fig. 10a). Because Athabasca River is fully frozen during the winter months, the contribution of discharge from the Athabasca River to the observed SCCF asymmetry would be minimal.

The complex hydrodynamics associated with LSL are a potential cause of the observed microseismic signals during winters. While the discussions of limnology and oceanography have been interleaving, the size, depth, stratification, surface movement, and bottom topography are substantially different between lakes and oceans (Kenney, 1991, 1996; Malm, 1999). Both human and environmental factors may be important in generating lake microseisms at LSL. As the largest lake fully contained in Alberta and one of Canada's most popular ice fishing sites, constant traffic on the frozen lake via various ice roads can cause significant vibrations on the lake ice layer. Vertical movements can easily be felt by a person standing on the ice surface and are capable of inducing turbulence beneath ice cap. Increased industrial traffic surrounding the lake during the winter months (e.g., freight trains and lakeside traffic) may also contribute to the episodic pressure changes within the ice-covered lake. However, the limited diurnal variation of the noise signals during the winter of 2008 (Fig. 10b) places rather restrictive timing constraints on these activities.

Natural causes of horizontal and/or vertical flow (Wuest and Lorke, 2003) beneath the 1–2-m-thick ice surface are a plausible cause of lake microseisms (Fig. 10c). Significant under-ice circulation has been previously reported in Tub Lake, Ontario (Colman and Armstrong, 1983), Wupaw Bay, Manitoba (Kenney, 1991, 1996), Harmon Lake, Ontario(Rogers and Lawrence, 1995), Lake Baikal, Siberia (Kelley, 1997), Vendyurskoe Lake, Karelia, Russia (Malm, 1999; Petrov *et al.*, 2007) and, in a slightly different setting, Hungry Horse reservoir in Montana (O'Connell, 2007). Based on information provided by a wide range of hydraulic measures, the strength of under-ice circulation of up to tens of millimeters per second are predicated on key attributes such as snow coverage, sediment heat flow (Rogers *et al.*, 1995; Kelley, 1997), ice- and water-layer thicknesses, and bottom topography (e.g., Polzin *et al.*, 1997). Substantial lateral variations of these parameters are expected over a large lake, especially for LSL, where the average depths of two approximately equal-area bays (connected by a narrow channel) differ by several meters. The substantial lake-bottom topography could facilitate turbulence and mixing, especially in the western bay, and cyroseisms (or frost quakes) due to extreme winter temperature variations are also conducive to the generation of internal waves (e.g., Polzin *et al.*, 1997; Malm, 1999). Once a source of excitation is present, LSL

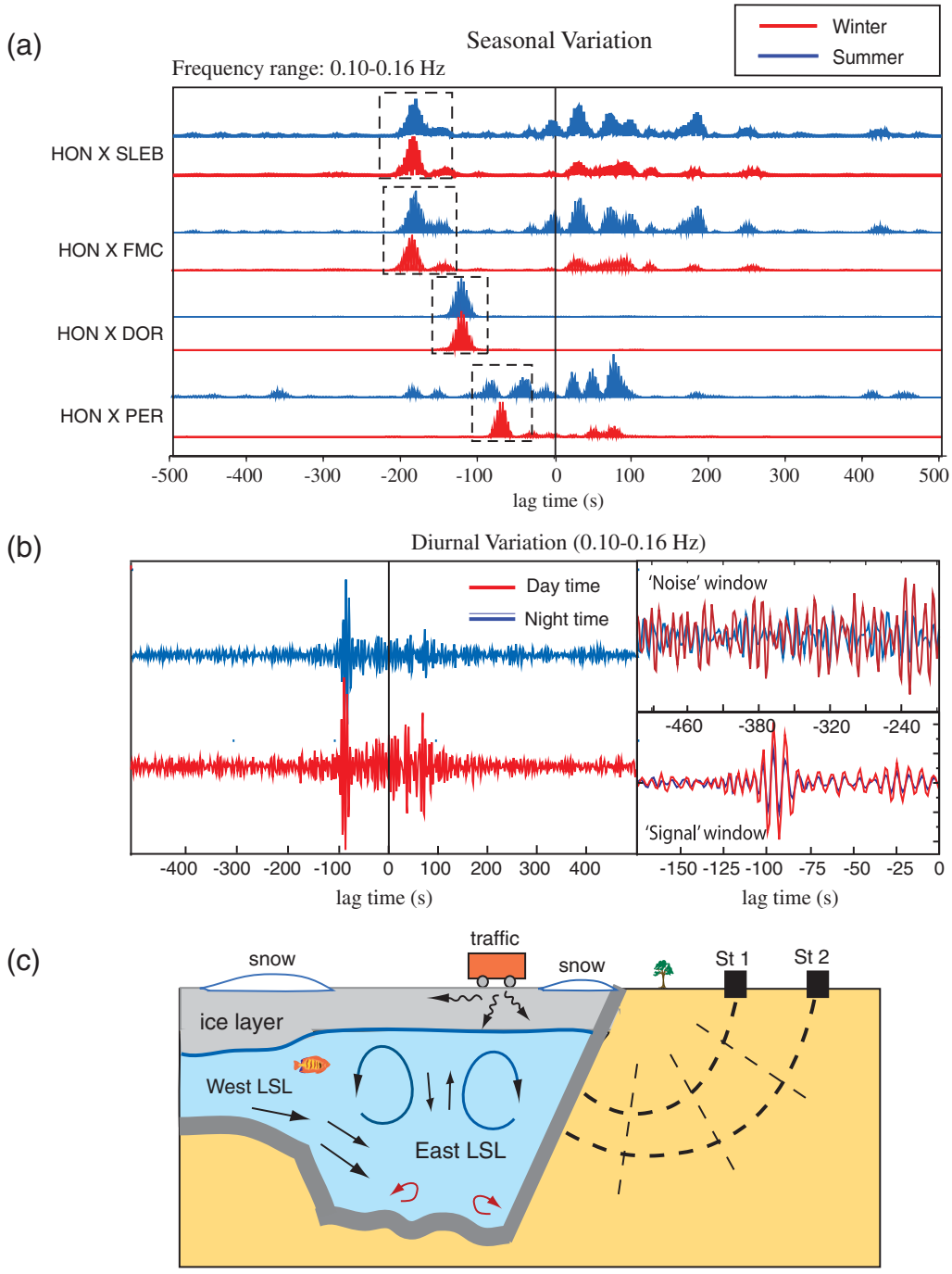

Figure 10. (a) Seasonal variations of the SCCFs in 2008. This one-year dataset is divided into two time periods (see main text) and the same correlation analysis is applied to each subset. In comparison with the summer months, the resulting SCCFs show much greater asymmetry during the winter of 2008. (b) Sample diurnal variations (for station pair HON and PER) during the winter months. The SCCFs are consistent between night and day, which suggest a common origin or mechanism. The signal part of the SCCFs (−150 s to 0 s, bottom right) are more consistent than the 'noise' part of the SCCFs (−500 s to −200 s), top right) for the daily analysis. The amplitudes have been self-normalized for both time windows. (c) A schematic diagram illustrating the potential origins of microseismic noise. Mixing and resonance, as well as human activities and environmental processes, may be responsible for the asymmetric SCCFs.

can act as a filter such that only certain modal frequencies (e.g., 0.06–0.2 Hz) are retained, resonated, and potentially amplified within the bounded system of ice, water, and sediment (see Fig. 10c).

Wind may also contribute to noise generation and the observed seasonal variations. According to the *Canadian Wind Energy Atlas* (see Data and Resources), the mean wind energy near LSL is ~700 W/m^2 and ~300 W/m^2 during the

winter and summer months of 2010, respectively (Fig. 11). Outside the foothills of the Rocky Mountains, the regional maximum due to pressure variations associated with extreme topographic relief, these levels are substantially larger than those of the surrounding regions including major water bodies 6–8 times larger in surface area (e.g., Great Slave Lake and Athabasca Lake) (see Fig. 11). Strong wind and ice storms would undoubtedly enhance ground motion in and around the lake, though it remains questionable whether the reported wind energy levels are sufficient to cause sustained microseismic signals near LSL.

Another key contributing factor to the observed seasonal variations is ground attenuation (e.g., Ardhuin *et al.*, 2011; Schimmel *et al.*, 2011). According to a recent study by Schimmel *et al.* (2011), low attenuation is largely responsible for strong SCCFs sampling old continents and isolated ocean islands (e.g., Hawaii). For the case of LSL, the amplitude and asymmetry of the SCCFs of the winter months could benefit from a weakly attenuating medium due to the solidification of muskegs (or, grassy bogs).

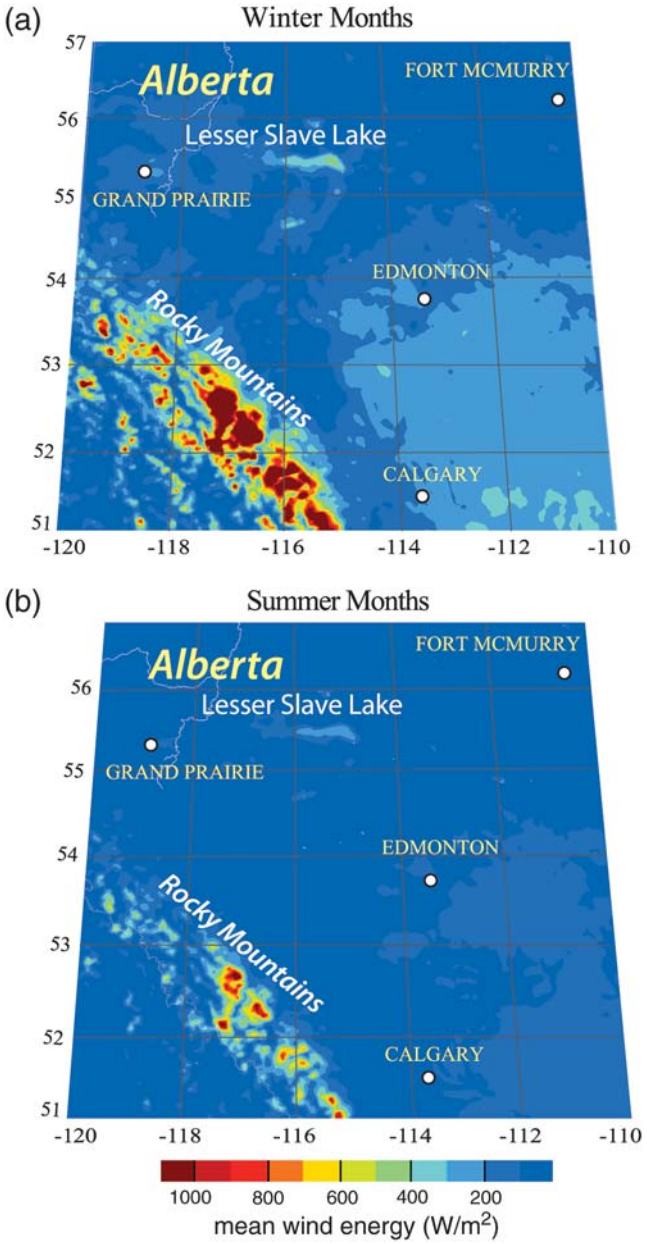

Figure 11. Mean wind energy during the (a) winter and (b) summer months of 2010 (see Data and Resources). Extreme values are observed along the Rocky Mountain front due to major topographic reliefs. Strong wind energy in the vicinity of LSL, which far exceeds those near water bodies of much greater sizes (e.g., Great Slave Lake, Athabasca Lake), could play a possible role in the generation of persistent local noise sources.

Conclusions

Based on asymmetrical seismic noise records from a local broadband array and multiple source migration methods, we are able to determine a persistent local noise source beneath the relatively quiet southern-central Alberta region. The peak of the effective probability function varies with assumed migration velocity and wave frequency, underscoring an estimated location uncertainty of ~100–150 km around LSL. The frequency of the asymmetric correlation window is consistent with those of global ocean microseisms.

The origin of this noise source remains inconclusive, though it is clear that the energy associated with the excitation can reach broadband seismic receivers several hundred kilometers away. We highlight lake microseisms as an intriguing possibility after reviewing various known mechanisms for regional noise generation. Our hypothesis is aided by the absence of known microseismic sources/mechanisms in the region and the spectral content of the asymmetric SCCFs, while limited observational and theoretical support, moderate source location uncertainty, and interfering ocean microseisms are legitimate concerns. Improved source location and characterization (e.g., Schimmel *et al.*, 2011), as well as a greater understanding of lake hydrodynamics, will be necessary to reliably determine the nature of the observed microseisms in southern-central Alberta.

Data and Resources

The main source of data (2007–2008) from CRANE can be requested through IRIS Data Management Center at www.iris.edu (last accessed January 2012). The data for the subsequent years are in the preparation stage for submission to IRIS for archival and public distribution. The Earthquake Canada database was searched using http://earthquakescanada.nrcan.gc.ca/index-eng.php (last accessed August 2011). Wind energy data and maps from the *Canadian Wind Energy Atlas* were retrieved from http://www.windatlas.ca/en/index.php (last accessed September 2011). Additionally, some plots in this study were made using the GMT mapping tools version 4.5.7 (Wessel and Smith, 1991).

Acknowledgments

We thank Sean Contenti and Ahmet Ökeler for insightful scientific suggestions. We also thank the staff members at CNSN for their generous assistance in retrieving continuous seismic data for part of this analysis, and for the helpful comments and suggestions from Martin Chapman and two anonymous reviewers. Above all, we are grateful to the host families of CRANE seismic stations for their support of our field project. This study is funded by the National Science and Engineering Council of Canada, Alberta Ingenuity, and the Canadian Foundation for Innovation.

References

Ardhuin, F., E. Stutzmann, M. Schimmel, and A. Mangeney (2011). Ocean wave sources of seismic noise, *J. Geophys. Res.* **116,** C09004, doi 10.1029/2011JC006952.

Bensen, G. D., M. H. Ritzwoller, M. P. Barmin, A. L. Levshin, F. Lin, M. P. Moschetti, N. M. Shapiro, and Y. Yang (2007). Processing seismic ambient noise data to obtain reliable broad-band surface wave dispersion measurements, *Geophys. J. Int.* **169**, doi 10.1111/j.1365-246X.2007.03374.x.

Brzak, K., Y. J. Gu, A. Ökeler, M. Steckler, and A. Lerner-Lam (2009). Migration imaging and forward modeling of microseismic noise sources near southern Italy, *Geochem. Geophys. Geosyst.* **10,** Q01012, doi 10.1029/2008GC002234.

Brooker, E. W., and R. B. Peck (1993). Rational design treatment of slides in overconsolidated clays and clay shales, *Can. Geotech. J.* **30,** 526–544.

Burtin, A., L. Bollinger, J. Vergne, R. Cattin, and J. L. Nábělek (2008). Spectral analysis of seismic noise induced by rivers: A new tool to monitor spatiotemporal changes in stream hydrodynamics, *J. Geophys.Res.* **113,** B05301, doi 10.1029/2007JB005034.

Chevrot, S., M. Sylvander, S. Benhamed, C. Ponsolles, J. Lefèvre, and D. Paradis (2007). Source location of secondary microseisms in western Europe: Evidence for both coastal and pelagic sources, *J. Geophys. Res.* **112,** B11301, doi 10.1029/2007JB005059.

Colman, J. A., and D. E. Armstrong (1983). Horizontal diffusivity in a small, ice-covered lake, *Limnol. Oceanogr.* **28,** 1020–1026.

Cruden, D. M., M. Ruel, and S. Thomson (1990). Landslides along the Peace River, Alberta, *43rd Can. Geotech. Conf. Proceed.* **1**, 61–68, 25–27 October 1990.

Davies, M. R., R. Paulen, and A. S. Hickin (2005). Inventory of Holocene landslides, Peace River area, Alberta (NTS 84C), Alberta Energy Utility Board, EUB/AGS Geo-Note 2003–43, 24 pages.

Frank, S. D., A. E. Foster, A. N. Ferris, and M. Johnson (2009). Frequency-dependent asymmetry of seismic cross-correlation functions associated with noise directionality, *Bull. Seismol. Soc. Am.* **99,** 462–470, doi 10.1785/0120080023.

Friedmann, S. J., G. Kwon, and W. Losert (2003). Granular memory and its effect on the triggering and distribution of rock avalanche events, *J. Geophys. Res.* **108,** B8, 2380, doi 10.1029/2002JB002174.

Gerstoft, P., and T. Tanimoto (2007). A year of microseisms in southern California, *Geophys. Res. Lett.* **34,** L20304, doi 10.1029/2007GL031091.

Gu, Y. J., C. Dublanko, A. Lerner-Lam, K. Brzak, and M. Steckler (2007). Probing the sources of ambient seismic noise near the coasts of southern Italy, *Geophys. Res. Lett.* **34,** L22315, doi 10.1029/2007GL031967.

Gu, Y. J., A. Ökeler, S. Contenti, K. Kocon, L. Shen, and K. Brzak (2009). Broadband seismic array deployment and data analysis in Alberta, *CSEG Recorder*, September, 37–44.

Gu, Y. J., A. Ökeler, L. Shen, and S. Contenti (2011). The Canadian Rockies and Alberta Network (CRANE): New constraints of the Rockies and Western Canada Sedimentary Basin, *Seismol. Res. Lett.* **82,** 575–588.

Gutenberg, G. (1931). Microseisms in North America, *Bull. Seismol. Soc. Am.* **21,** 1–24.

Hasselmann, K. (1963). A statistical analysis of the generation of microseisms, *Rev. Geophys.* **1,** 177–210, doi 10.1029/RG001i002p00177.

Haubrich, R. A., and K. McCamy (1969). Microseisms: Coastal and pelagic sources, *Bull. Seismol. Soc. Am.* **7,** 539–571.

Hughes, B. (1976). Estimates of underwater sound (and infrasound) produced by nonlinearly interacting ocean waves, *J. Acoust. Soc. Am.* **60,** 1032–1039.

Kedar, S., M. Longuet-Higgins, F. Webb, N. Graham, R. Clayton, and C. Jones (2008). The origin of deep ocean microseisms in the North Atlantic Ocean, *Proceedings of the Royal Society London–Series A: Containing Papers of a Mathematical and Physical Character* **464,** 1–35, doi 10.1098/rspa.2007.0277.

Kelley, D. E. (1997). Convection in ice-covered lakes: Effects on algal suspension, *J. Plankton Res.* **19,** 1859–1880.

Kenney, B. C. (1991). Under-ice circulation and the residence time of a shallow bay, *Can. J. Fish. Aquat. Sci.* **48,** 152–162.

Kenney, B. C. (1996). Physical limnological processes under ice, *Arch. Hydrobiol.* **322,** 85–90.

Kerman, B. R., and R. F. Mereu (1993). Wind-induced microseisms from Lake Ontario, *Atmosphere-Ocean* **31,** 501–516.

Koper, K. D., K. Seats, and H. Benz (2010). On the composition of Earth's short-period seismic noise field, *Bull. Seismol. Soc. Am.* **100,** 606–617, doi 10.1785/0120090120.

Kvarnas, H. (2001). Morphometry and Hydrology of the four large lakes of Sweden, *AMBIO: A Journal of the Human Environment* **30,** 467–474.

Longuet-Higgins, M. (1950). A theory of the origin of microseism, *Phil. Trans. Roy. Soc. Lond.* **243,** 1–35.

Lynch, J. (1956). The Great Lakes, a source of two-second frontal microseisms, *Travaux Sci.* **19,** 177–182.

Malm, J. (1999). Some properties of current and mixing in an ice-covered lake, *Water Resources Res.* **35,** 221–232.

Mansour, M. F. (2009). Characteristic behavior of slow moving slides, *Ph.D. Thesis* University of Alberta, Alberta, Canada, 293 pages.

Morgan, A. J., R. C. Paulen, and C. R. Froese (2008). Ancestral buried valleys of the Peace River: Effects on the town of Peace River, *Proceed. 61st Can. Geotech. Conf.*, Edmonton, Alberta, Canada, 1219–1226.

O'Connell, D. R. H. (2007). Concrete dams as seismic imaging sources, *Geophys. Res. Lett.* **34,** L20307, doi 10.1029/2007GL031219.

Patterson, J. C., and P. F. Hamblin (1988). Thermal simulation of a lake with winter ice cover, *Limnol. Oceanogr.* **33,** 323–338.

Paul, P., M. Campillo, L. Margerin, E. Larose, and A. Derode (2005). Empirical synthesis of time-asymmetrical Green functions from the correlation of coda waves, *J. Geophys. Res.* **110,** doi 10.1029/2004JB003521.

Pawlak, A., D. W. Eaton, I. D. Bastow, J.-M. Kendall, G. Helffrich, J. Wookey, and D. Snyder (2011). Crustal structure beneath Hudson Bay from ambient-noise tomography: Implications for basin formation, *Geophys. J. Int.* **184,** 65–82.

Petrov, M. P., A. Y. Terzhevik, R. E. Zdorovennov, and G. E. Zdorovennova (2007). Motion of water in an ice-covered shallow lake, *Water Resour.* **34,** 113–122.

Polzin, K. L., J. M. Toole, J. R. Ledwell, and R. W. Schmitt (1997). Spatial variability of turbulent mixing in the abyssal ocean, *Science* **276,** 93–95.

Pedrazzini, A., M. Jaboyedoff, C. Froese, W. Langenberg, and F. Moreno (2008). Structures and failure mechanisms analysis of Turtle Mountain, *Proceed. 4th Can. Conf. Geohazards*, Presse de l'Université Laval, Québec, Canada, 594 pages.

Rhie, J., and B. Romanowicz (2006). A study of the relation between ocean storms and the Earth's hum, *Geochem. Geophys. Geosyst.* **7,** Q10004, doi 10.1029/2006GC001274.

Rogers, C. K., G. A. Lawrence, and P. F. Hamblin (1995). Observations and numerical simulation of a shallow ice-covered midlatitude lake, *Limnol. Oceanogr.* **40,** 374–385.

Sabra, K. G., P. Gerstoft, P. Roux, W. A. Kuperman, and M. C. Fehler (2005). Extracting time-domain Green's function estimates from ambient seismic noise, *Geophys Res. Lett.* **32,** L03310, doi 10.1029/2004GL021862.

Schulte-Pelkum, V., P. S. Earle, and F. L. Vernon (2004). Strong directivity of ocean-generated seismic noise, *Geochem. Geophys. Geosyst.* **5,** Q03004, doi 10.1029/2003GC000520.

Schimmel, M., E. Stutzmann, F. Ardhuin, and J. Gallart (2011). Polarized Earth's ambient microseismic noise, *Geochem. Geophys. Geosyst.* **12,** doi 10.1029/2011GC003661.

Shapiro, N. M., M. Campillo, L. Stehly, and M. H. Ritzwoller (2005). High resolution surface wave tomography from ambient seismic noise, *Science* **307,** 1615–1618.

Shapiro, N. M., M. H. Ritzwoller, and G. D. Bensen (2006). Source location of the 26 sec microseism from cross-correlations of ambient seismic noise, *Geophys. Res. Lett.* **33,** L18310, doi 10.1029/2006GL027010.

Stehly, L., M. Campillo, and N. Shapiro (2006). A study of the seismic noise from its long-range correlation properties, *J. Geophys. Res.* **111,** B10306, doi 10.1029/2005JB004237.

Stern, V. H., and Y. J. Gu (2011). Documenting Alberta seismicity with BRTT's Antelope software, *5th Can. Conf. Geotech. Natural Hazard*, Kelowna, British Columbia, 7 pages.

Suda, N., K. Nawa, and Y. Fukao (1998). Earth's background free oscillations, *Science* **279,** 2085–2091.

Tanimoto, T., J. Um, K. Nishida, and N. Kobayashi (1998). Earth's continuous oscillations observed on seismically quiet days, *Geophys Res. Lett.* **25,** 1553–1556.

Tikku, A. A., D. C. McAdoo, M. S. Schenewerk, and E. C. Willoughby (2006). Temporal fluctuations of microseismic noise in Yellowstone's Upper Geyser Basin from a continuous gravity observation, *Geophys. Res. Lett.* **33,** L11306, doi 10.1029/2006GL026113.

Webb, S. C. (2007). The Earth's 'hum' is driven by ocean waves over the continental shelves, *Nature* **445,** doi 10.1038/nature05536.

Weichert, D. H., and M. Henger (1976). The Canadian seismic array monitor processing systeni (CANSAM), *Bull. Seismol. Soc. Am.* **66,** 1381–1403.

Wessel, P., and W. H. F. Smith (1991). Free software helps map and display data, *Eos. Trans. AGU* **72,** no. 441, 445–446.

Wuest, A., and A. Lorke (2003). Small-scale hydrodynamics in lakes, *Annu. Rev. Fluid Mech.* **35,** 373–412.

Yang, Y., and M. Ritzwoller (2008). Characteristics of ambient seismic noise as a source for surface wave tomography, *Geochem. Geophys. Geosyst.* **9,** Q02008, doi 10.1029/2007GC001814.

Yang, Y., M. H. Ritzwoller, A. L. Levshin, and N. M. Shapiro (2007). Ambient noise Rayleigh wave tomography across Europe, *Geophys. J. Int.* **168,** 259–274.

Yao, H., and R. D van der Hilst (2009) Analysis of ambient noise energy distribution and phase velocity bias in ambient noise tomography, with application to SE Tibet, *Geophys. J. Int.* **179,** doi 10.1111/j.1365-246X.2009.04329.x.

Yilmaz, O. (2001). Seismic data analysis: Processing, inversion, and interpretation of seismic data, volume II, *Investigations in Geophysics* **10**, Society of Exploration Geophysics, Tulsa, Oklahoma, 2027 pages.

Department of Physics
University of Alberta
Edmonton, Alberta, T6G2E1
ygu@ualberta.ca

Manuscript received 10 January 2010